Published in final edited form as:
J Mater Res. 2008 February 1; 23(2): 478–485. doi:10.1557/JMR.2008.0051.

Ultrastructural analyses of nanoscale apatite biomimetically grown on organic template

S.I. Hong[a],
Department of Biologic and Materials Sciences, University of Michigan, Ann Arbor, Michigan 48109-1078; and Department of Nano-materials Engineering, Chungnam National University, Taejon, 305-764, Korea

K.H. Lee,
Department of Nano-materials Engineering, Chungnam National University, Taejon, 305-764, Korea

M.E. Outslay, and
Department of Biomedical Engineering, University of Michigan, Ann Arbor, Michigan 48109-2099

D.H. Kohn
Department of Biologic and Materials Sciences, University of Michigan, Ann Arbor, Michigan 48109-1078; and Department of Biomedical Engineering, University of Michigan, Ann Arbor, Michigan 48109-2099

Abstract

The ultrastructure of nanoscale apatite biomimetically formed on an organic template from a supersaturated mineralizing solution was studied to examine the morphological and crystalline arrangement of mineral apatites. Needle-shaped apatite crystal plates with a size distribution of ~100 to ~1000 nm and the long axis parallel to the *c* axis ([002]) were randomly distributed in the mineral films. Between these randomly distributed needle-shaped apatite crystals, amorphous phases and apatite crystals (~20–40 nm) with the normal of the grains quasi-perpendicular to the *c* axis were observed. These observations suggest that the apatite film is an interwoven structure of amorphous phases and apatite crystals with various orientations. The mechanisms underlying the shape of the crystalline apatite plate and aggregated apatite nodules are discussed from an energy-barrier point of view. The plate or needle-shaped apatite is favored in single-crystalline form, whereas the granular nodules are favored in the polycrystalline apatite aggregate. The similarity in shape in both single-crystalline needle-shaped apatite and polycrystalline granular apatite over a wide range of sizes is explained by the principle of similitude, in which the growth and shape are determined by the forces acting upon the surface area and the volume.

I. INTRODUCTION

Using a biomimetic approach to induce calcium–phosphate deposition from supersaturated solutions of simulated body fluid (SBF), bone-like apatite can be deposited on metals, ceramics, glasses, and polymers.[1–7] Currently, this method is used to coat permanent implants[1–4] with the aim of improving biological compatibility and osteoconductivity, as well as degradable scaffolds that support skeletal tissue repair and regeneration.[5–8] Because direct bonding between an implant and bone can occur if a layer of bone-like mineral forms on the surface of the implant,[9] it has been hypothesized that the formation of such a mineral layer within the

aAddress all correspondence to this author. sihong@cnu.ac.kr, sihong@umich.edu.

pores of a scaffold may enhance the conduction of host cells into the scaffold and also enhance the osteogenic differentiation of transplanted cells.[6] Because changes in mineral composition, structure, and morphology lead to biological changes in vitro and in vivo, the material characterization of the mineral layer interfacing with the biological milieu is of importance.

The macroscopic and nanoscopic morphology of apatite coatings deposited from SBF are influenced by calcium and phosphate concentration, pH, temperature, and the presence of other inorganic and organic molecules.[3,10–12] The morphology and structure of apatites, in turn, dictate the biomechanical and biochemical properties.[2,3,5,13–16] However, few ultrastructural-level studies (from 0.1 to 100 nm) on apatite films deposited from SBF have been conducted, and most transmission electron microscopy (TEM) studies have been performed on apatite powders or precipitates processed by methods that are subject to limitations. For example, Lu and Leng[13] prepared TEM specimens by extracting the deposited film by an ultrasonic vibration method, and Chou et al.[3] prepared specimens by scraping off the deposited film, suspending apatite precipitates in isopropanol, and picking them up on Cu grids. It is difficult using these TEM specimen preparation methods to observe thick films (from >100 nm up to ~1 mm), which may have different morphological and crystalline arrangements from those of the initially nucleated film (which is thin enough to be electron transparent), without further thinning. Various phases such as amorphous calcium phosphate (ACP), dicalcium phosphate (DCPD), octacalcium phosphate (OCP), and hydroxyapatite (HA) were reported to be formed in the biomimetically formed mineral film, and the phases transform with time and the thickness of the mineral film.[10] In general, the phases with lower energy barriers for nucleation are formed initially, but they transform to the phases with lower free energies. Apatite is known to have a higher energy barrier for nucleation than other forms of calcium phosphates such as ACP, DCPD, and OCP. Therefore, the initially nucleated film is likely to be composed of metastable phases, and the microstructure of the initially nucleated thin mineral film may not truly represent the stabilized microstructure.

The crystal structure and orientation, morphology, and phase distribution of biomimetically deposited films are not well understood compared with those of synthetic apatites processed by conventional means or natural apatite.[10–15] Furthermore, recent studies[3,13] on the nano-structure of mineral films deposited from SBF report different crystal structures and morphologies, suggesting a more complicated nature for apatite crystal growth from SBF than synthetic apatite. For example, Lu and Leng[13] reported that they observed ACP and granular OCP, instead of apatite, which is in contrast with the observation of the plate-like and needlelike apatite reported by Chou et al.[3]

The objective of this study was to analyze the ultra-structure of calcium phosphate films biomimetically deposited onto poly(lactide-*co*-glycolide) (PLGA) substrates from SBF using high-resolution electron transmission microscopy (HRTEM). The SBF used in this study was a modified solution, with a concentration of Ca^{2+} and HPO_4^{2-} ions twice as high as those in human blood plasma to accelerate the biomimetic process, and the thick mineral films (>100 μm) with a stabilized structure were used for nanostructural analyses. Emphasis was placed on the morphological and crystalline arrangement of various phases of calcium phosphate to understand the mechanism underlying the shape of apatite and/or other calcium phosphate crystals in the fully grown films (>100 μm).

II. EXPERIMENTAL

Rectangular glass plates, 20 mm × 20 mm × 1 mm, were coated with a solution of 5 wt% PLGA with a lactic/glycolic ratio of 85:15 (Medisorb, Cincinnati, OH), dissolved in chloroform, as previously described,[17] and used as a substrate for apatite deposition. The SBF was prepared by dissolving chemicals into deionized water in the sequence of 141 mM NaCl, 4.0 mM KCl,

0.5 mM $MgSO_4$, 1.0 mM $MgCl_2$, 4.2 mM $NaHCO_3$, 5.0 mM $CaCl_2$–$2H_2O$, and 2.0 mM KH_2PO_4, and titrating to pH 6.8 with NaOH at 25 °C. The SBF used in this study was a 1× modified solution, with the concentration of Ca^{2+} and HPO_4^{2-} ions twice as high as those of human blood plasma.[17] The PLGA-coated glass was immersed in the SBF and kept in an incubator at 37 °C. The SBF was refreshed every day for 7 days to replenish the ion concentration to supersaturated levels. Fourier transform infrared (FTIR) spectroscopy (Spectrum BX FT-IR; Perkin-Elmer, Norwalk, CT) was performed for substructural and band analyses. Mineralized specimens were coated with a thin layer of gold and were observed under a scanning electron microscope (SEM) (Topcon, Japan, SM-500); to identify surface morphology on a scale of 0.1–100 μm.

For HRTEM observations, biomimetically deposited films were detached by breaking or dissolving PLGA between the calcium phosphate layer and the glass plate. Pieces (width 3–8 mm, thickness ~100 μm) of detached films were broken into smaller pieces by bending, were placed on a Cu grid with a hole (typically 1 mm in diameter), and were attached using silver conductive adhesive in the center of Cu grid (completely covering the hole). Cu grids with calcium phosphate flakes were then ion milled on both sides to get the thin area in the middle, away from both surfaces, on a liquid nitrogen stage at 5 kV using an incidence angle of 11–12°. To prevent damage to the specimens, ion milling was performed below −100 °C.[18] To ensure the samples were adequately cooled before ion milling, the specimen rotation drive rod was submerged in liquid nitrogen for at least 1 h prior to ion milling. To get a large thin area on the mineral film, a laser terminator was used to cut off the power of the ion miller as soon as a hole was produced. The mineral films were thinned to <100 nm by thinning both the top and bottom surfaces using the ion-milling method on a cold stage. The arrangement and structure of stabilized phases present in the mineral film can be observed in this method.

HRTEM observations and selected-area diffraction (SAD) analyses of bone-like mineral and bone were carried out using a Jeol (Tokyo, Japan) JEM 2010 transmission electron microscope operated at 200 kV. Using digitized images and data, fast Fourier transform (FFT) patterns with noise filtering were obtained and analyzed.[18]

III. RESULTS

After seven days of immersion in 1× modified SBF, PLGA substrates were completely coated with calcium phosphate. At a low magnification [Fig. 1(a)], a conglomerated granular structure with needle-shaped precipitates was clearly visible. At a higher magnification, the surfaces consisted of elongated thin plates grown out of the surface of the granular structures. FTIR spectra (Fig. 2) exhibited a broad band for O–H, ranging from 3000 to 3700 cm^{-1}; a peak for O–H at 1650 cm^{-1}; peaks for P–O at 1270, 1185, 1080, 960, and 603 cm^{-1}; and peaks for C–O at 1551, 1460, and 863 cm^{-1}. The presence of C–O indicates that the calcium phosphate is carbonated apatite.[3,5,17] The carbonate content in the apatite prepared by this method is in the range of 3–8 wt%,[5] equivalent to the carbonate content of bone.

Ultrastructural images obtained by HRTEM [Figs. 3(a) and 3(b)] clearly display needlelike apatite, with needle lengths ranging from ~1000 [Fig. 3(a)] down to ~100 nm [Fig. 3(b)]. The longer apatite needles were straight [Fig. 3(a)], whereas smaller needles (~100–200 nm) were curved [Fig. 3(b)]. The needlelike apatite observed by HRTEM is thought to be the cross-sectional image of the plate-like apatite crystals observed under the SEM [Fig. 1(b)]. The contrast of the regions surrounded by the needlelike apatite crystals was gray compared to the dark images of the needles, suggesting that the regions surrounded by needles are either apatite with a different orientation or a phase with different crystalline structure.

The SAD pattern (Fig. 4) matched with indices that were obtained from HA. Although the carbonate substitution in Type B carbonate apatites causes a change of lattice constants (i.e., a decrease in the *a* axis and an increase in the *c* axis),[19] the change of lattice constants for the carbonated apatite of 3–8% is so small that a difference in diffraction patterns from those of pure HA could not be identified. The rings with double and triple indices indicate that those planes have interplanar spacings that are so close that they cannot be separated into separate rings in the diffraction pattern. The continuous rings suggest that the coating consists of a great number of different crystals. It should be noted that (002) rings are also continuous, suggesting that the apatite crystals have the *c* axis parallel to the plane of the view, but with rotational freedom in this plane.

Figure 5(a) shows bright-field and Fig. 5(b) dark-field images taken from the same area of a sample. The dark-field image in Fig. 5(b) was obtained by placing the objective aperture on the spot of the (002) ring in the inset diffraction pattern of Fig. 5(a). Most needles on the right-hand side of Fig. 5 were highlighted, suggesting that they have ⟨002⟩ direction parallel to the plane of the image in Fig. 5. Occasionally, bright round spots [marked with white arrows in Fig. 5(b)] were observed in the central region surrounded by needles, suggesting that there are a small number of circular grains with crystalline orientation similar to that of the needles. Because the diffraction rings matched with those of apatite and no other diffraction rings were observed, the dark regions surrounded by highlighted needles [Fig. 5(b)] are likely apatites with different orientations and some amorphous phase, as confirmed by the HRTEM images.

The HRTEM images also exhibited the same lattice fringe image through a needle, revealing that most needles are single crystalline. A scissors-shaped apatite, two needles joined together in the middle, is shown (Fig. 6). A crystalline lattice image is clearly visible in the needle, and the axis of each needle is parallel to the *c* axis [(002) direction] of the hexagonal structure. The transverse direction of the needles is parallel to the (100) direction. The spacings between the (002) and (100) planes were measured to be 0.34 and 0.82 nm, respectively. It is interesting to note that each shear of the scissors is single crystalline and that they form a low-angle boundary (3°–4°) at the point where they join each other because of their misorientation with respect to each other. It is not clear whether the two shears joined after they nucleated and grew independently or whether they branched from one crystal. Nonetheless, it is clear that each needle-shaped apatite is single crystalline.

Some regions surrounded by needle-shaped plates exhibited granular apatites (marked with “A”, “B,” and “C” Fig. 7) and ACP (indicated by white arrows). The FFT patterns from grains A and B revealed that the zone axis of grain A is [110] and that of grain B is [013]. Therefore, the angle between the zone axis of grain A and the *c* axis of the hexagonal structure is zero, and that of grain B and the *c* axis is 85.4°. Grain C has a similar orientation to grain B, but with a rotational symmetry. The presence of A-type grains with the *c* axis parallel to the substrate is limited, as evidenced by the dark region surrounded by highlighted needles in the dark-field image [Fig. 5(b)]. Most grains in the central region surrounded by needle-shaped apatites have an amorphous phase or a different crystallographic orientation than the needle-shaped apatites and are mostly oriented with the *c* axis quasi-perpendicular to the substrate. This orientation difference explains why the central region surrounded by needle-shaped plates was mostly dark in the dark-field image [Fig. 5(b)] obtained from that part of the (002) ring.

ACP is not a major component of the mineral but is observed in limited regions (Fig. 8). ACP is thought to be formed at the beginning of the deposition due to a lower surface energy than OCP and apatite.[20] There are small crystalline particles (parallel lines identified with arrows) with a size of 2–3 nm. The FFT pattern (Fig. 8, inset) also exhibited a halo from ACP and some discrete spots from the crystalline phases. The spacing between lattice fringes of crystalline particles was in the range of 0.27–0.29 nm. Because the lattice spacing of the small particles

was similar to those of (112) or (211) planes, they are most likely apatite crystals crystallized from ACP. The exact orientation of the particles in Fig. 8 could not be unambiguously identified because of the small size of the particles. Because the critical diameter for the stability of an apatite nucleus was estimated to be 1 nm,[21] the particles shown in Fig. 8 are thought to be close to the nuclei of apatites.

IV. DISCUSSION

The presence of needle-shaped apatite crystals with a wide range of sizes (100–1000 nm) suggests that apatite crystals grow with time following initiation onto the substrate. The similarity in shape over a wide range of sizes can be explained by the principle of similitude, which suggests that the growth, decay, and shape of any structure are determined by the forces acting upon it.[22,23] Thomson[23] suggested that a common shape across different scales is due to the fact that some physical forces act in proportion to surface area, while others are proportional to the volume of the body. Scaling has a physical significance in that the underlying mechanisms of a given process can be assumed to be unchanged over the regime in which the scaling holds.[23,24] The principle of similitude has been observed in many biological[22–24] and materials[25–27] systems. The forces associated with surface area and volume in determining the shape of apatite crystals will be discussed below.

The biomimetically deposited mineral consists of differently oriented carbonated apatite crystals and some ACP. Needle-shaped apatite is oriented with the *c* axis parallel to the long axis of the needles. The observation that needle-shaped apatite is single crystalline is compatible with the recent study of Aiziwa et al.[15] on synthetic carbonate-containing apatite fibers. The regions surrounded by needle-shaped apatite exhibit amorphous phases and crystalline grains with the *c* axis mostly quasi-perpendicular to the long axis of the needle-shaped plates (which are parallel to the plane of the substrate). These observations suggest that the mineral film is an interwoven structure of an amorphous phase and apatite crystals with various orientations.

The presence of continuous (002) rings has been observed in some biomimetically grown mineralized films.[2,28] The random distribution of needle-shaped plates with the *c* axis parallel to the long axis on the plane of the view [Fig. 3(b)] is compatible with the appearance of a continuous (002) ring (Fig. 4). This observation is in contrast with that of lamellar bone[29] in which a partial (002) ring was observed, indicating a preferred orientation of needle-shaped apatite plates. However, a continuous (002) ring was observed in murine trabecular bone[30,31] and human dentin.[32] The difference in orientation distribution of apatite crystals among different systems may be associated with a stress effect. The arrangement of apatite crystals aligned along the principal stress direction is well known.[33,34] The trabecular bone in the proximal femur is subjected to a more complex stress state than the lamellar bone in the mid-diaphysis.[30,31,34] In the case of trabecular bone and dentin in which the major stress components are multidirectional, the apatite crystals need to be oriented such that they can resist the load from multiple directions,[30,31] resulting in no pronounced preferred orientation distribution of apatites. The principal stress component of lamellar bone in the mid-diaphysis is mostly uniaxial (parallel to the long axis), and apatite crystals are aligned along the long axis of the bone. Because the apatite crystals formed in SBF experience no other major external stresses, the needle-shaped crystals have no preferred orientation in the plane of the film.

The mineral apatite in bone is plate-shaped with the *c* axis parallel to the long axis of the mineral plate,[30,31,35,36] which suggests that the needles and/or plates are thermodynamically favorable. Because the *c* axis (0.688 nm) is shorter than the *a* axis (0.942 nm) in the hexagonal structure of HA, the planar density of calcium is smaller in the plane perpendicular to the *c* axis. One consequence of the anisotropic distribution of atoms is the orientation dependence of surface

energy, which is dependent on the orientation dependence of the bonding strength of crystalline apatite. The observation[15] that apatite fibers cleave along the long axis (which is parallel to the *c* axis) when they are fractured suggests that apatite is weak along the planes oriented parallel to the *c* axis.[15] Because the fracture work of brittle materials is dominated by the surface energy,[37,38] cleavage along the *c* axis[15] suggests that the surface energy of the planes parallel to the *c* axis is lower than that of the basal plane of the hexagonal structure of apatite. Apatite plates on the surface [Fig. 1(b)] were nucleated from solution; therefore, the strain energy due to the volume change and the strain mismatch between different lattices during precipitation is not likely to play a major role. Therefore, the predominant energy barrier for the nucleation and growth of apatite plates near the surface is thought to be the surface energy. The nucleation and growth of plate or needle-shaped apatite with the long axis parallel to the *c* axis are compatible with the suggestion that the plane parallel to the *c* axis in apatite single crystals has a lower surface energy. The plate or needle-shaped apatite is thus favored in single-crystalline apatites from the energy-barrier point of view.

Another interesting observation is the nodular apatite grains [Fig. 1(a)] at a low magnification despite the plate-type crystals [Fig. 1(b)] on the more microscopic scale. The formation of granular apatite nodules also can be explained in terms of surface-energy criteria. The mineral film consists of differently oriented apatite crystals and some ACP, which can be considered to be isotropic on a macroscale. In this case, the surface energy of the polycrystalline apatite nodules (with some amorphous regions) can be considered to be isotropic in contrast to anisotropic surface energy in plate-type monocrystalline apatite. The sphere-type apatite nodules are favored to reduce the surface area in polycrystalline form.

We note the similarity in shape and orientation between the biomimetically deposited apatite[28] and trabecular bone.[30,31,39] The diffraction patterns from murine trabecular bone[30,31,40] exhibit continuous rings of (002), (210), (112), (310), (222), (123), and (004), matching the rings observed in the present study. The orientation of the needle-shaped plates observed in this study is therefore similar to that of trabecular bone.[30,31,40] The similarity in crystalline arrangement and morphology between plate-type apatite in bone and biomimetic apatite reported in other studies[10,11,28,30,31,41–43] also supports the principle of similitude in apatite formation.

V. CONCLUSIONS

Apatite films biomimetically nucleated and grown on PLGA substrates consisted of differently oriented carbonated apatite crystals and some ACP. Needle-shaped apatite was single crystalline. The biomimetically formed mineral is an interwoven structure of amorphous phases and apatite crystals with various orientations. Plate or needle-shaped apatites are favored in single-crystalline apatites from energy-barrier point of view. The conglomeration of apatites can be considered to be isotropic on a macroscale, and the surface energy, therefore, can be reduced by forming nodular apatite grains on a larger scale. The similarity in shape either in single-crystalline needle-shaped apatite or polycrystalline granular apatite over a wide range of sizes conforms to the principle of similitude in which the growth and shape are determined by the forces acting upon the surface area and the volume.

Acknowledgments

We acknowledge the support from National Institutes of Health Grants R01 DE 013380 and DE 015411 (to D.H. Kohn). S.I. Hong is grateful for support from the Korea Research Foundation (2004-D00318).

References

1. Bunker BC, Rieke PC, Tarasevich BJ, Campbell AA, Fryxell GE, Graff GL, Song L, Liu J, Virden JW, McVay GL. Ceramic thin-film formation on functionalized interfaces through biomimetic processing. Science 1994;264:48. [PubMed: 17778133]
2. Tanahashi M, Kokubo T, Nakamura T, Katsura Y, Nagano M. Ultrastructural study of an apatite layer formed by biomimetic process and its bonding to bone. Biomaterials 1996;17:47. [PubMed: 8962947]
3. Chou YF, Chiou WA, Xu Y, Dunn JCY, Wu BM. The effect of pH on the structural evolution of accelerated biomimetic apatite. Biomaterials 2004;25:5323. [PubMed: 15110483]
4. Vasudev DV, Ricci JL, Sabatino C, Li P, Parsons R. In vivo evaluation of a biomimetic apatite coating grown on titanium surfaces. J Biomed Mater Res 2004;69A:629.
5. Murphy WL, Kohn DH, Mooney DJ. Growth of continuous bone-like mineral within porous poly (lactic-co-glycolic acid) scaffolds in-vitro. J Biomed Mater Res 2000;50:50. [PubMed: 10644963]
6. Kohn, DH.; Shin, K.; Hong, SI.; Jayasuriya, AC.; Leonova, EV.; Rossello, RA.; Krebsbach, PH. Self-assembled mineral scaffold as a model systems for biomineralization and tissue engineering. In: Landis, WJ.; Sodek, J., editors. Proceedings of 8th International Conference on the Chemistry and Biology of Mineralized Tissue; Toronto, ON, Canada: University of Toronto Press; 2005. p. 216
7. Müller L, Müller FA. Preparation of SBF with different HCO_3 content and its influence on the composition of biomimetic apatites. Acta Biomater 2006;2:181. [PubMed: 16701876]
8. Yang XB, Green DW, Roach HI, Clarke NM, Anderson HC, Howdle SM, Shakesheff KM, Oreffo RO. Novel osteoin-ductive biomimetic scaffolds stimulate human osteoprogenitor activity-implications for skeletal repair. Connect Tissue Res 2003;44(Suppl 1):312. [PubMed: 12952215]
9. Hench LL. Bioceramics: From concept to clinic. J Am Ceram Soc 1991;74:1487.
10. Eanes, ED. Dynamics of calcium phosphate precipitation. In: Bonucci, E., editor. Calcification in Biological Systems. CRC Press; Boca Raton, FL: 1992. p. 1
11. LeGeros, RZ. Calcium Phosphates in Oral Biology and Medicine. Karger; Basel, Switzerland: 1991. p. 12
12. Janasova L, Muller FA, Helebrant A, Strnad J, Greil P. Biomimetic apatite formation on chemically treated titanium. Biomaterials 2004;25:1187. [PubMed: 14643592]
13. Lu X, Leng Y. TEM study of calcium phosphate precipitation on bioactive titanium surfaces. Biomaterials 2004;25:1779. [PubMed: 14738841]
14. Layani JD, Guisinier FJG, Steuer P, Cohen H, Voegel JC, Mayer I. High resolution electron microscopy study of synthetic carbonate and aluminum containing apatites. J Biomed Mater Res 2000;50:199. [PubMed: 10679685]
15. Aizawa M, Porter AE, Best SM, Bonfield W. Ultrastructural observation of single crystal apatite fibers. Biomaterials 2005;26:3427. [PubMed: 15621231]
16. Leng Y, Chen J, Qu S. TEM study of calcium phosphate precipitation on HA/TCP ceramics. Biomaterials 2003;24:2125. [PubMed: 12699649]
17. Luong LN, Hong SI, Patel RJ, Outslay ME, Kohn DH. Spatial control of protein within biomimetically nucleated mineral. Biomaterials 2006;27:1175. [PubMed: 16137760]
18. Lee KH, Hong SI. Interfacial and twin boundary structures of nanostructured Cu-Ag filamentary composites. J Mater Res 2003;18:2194.
19. LeGeros RZ, LeGeros JP, Trautz OR, Klein E, Shirra WP. Conversion of monetite, $CaHPO_4$ to apatites: Effect of carbonate on the crystallinity and the morphology of the appatite crystallites. Adv X-ray Anal 1971;14:57.
20. Eanes ED, Termine JD, Nylen MU. An electron microscope study of the formation of amorphous calcium phosphate and its transformation to crystalline apatite. Calcif Tissue Res 1973;12:143. [PubMed: 4710793]
21. Eanes ED, Poster AS. A note on the crystal growth of hydroxyapatite precipitated from aqueous solutions. Mater Res Bull 1970;6:377.
22. Tomalin RC. The principle of similitude. Phys Rev 1914;3:244.
23. Thomson, DW. On Growth and Form. Cambridge University Press; Cambridge, UK: 1961.

24. Weibel EW. Fractal geometry: A design principle for living organisms. Am J Physiol Lung Cell Mol Physiol 1991;261:L361.
25. Hong SI. Influence of dynamic strain aging on the dislocation structure. Mater Sci Eng 1986;79:1.
26. Godfrey A, Hughes DA. Physical parameters linking deformation microstructures over a wide range of length scale. Scripta Mater 2004;51:831.
27. Hong SI, Kwon HJ. Superplasticity of Cu-Ag microcomposites. J Mater Res 2001;16:1822.
28. Luong LN, Hong SI, Patel RJ, Outslay ME, Kohn DH. Spatial control of protein within biomimetically nucleated mineral. Biomaterials 2006;27:1175. [PubMed: 16137760]
29. Rindby A, Voglis P, Engstrom P. Microdiffraction studies of bone tissues using synchrotron radiation. Biomaterials 1998;19:2083. [PubMed: 9870760]
30. Hong, SI.; Hong, SK.; Kohn, DK. Nanostructural analysis of murine femoral trabecular bone. University of Michigan; 2007. unpublished study
31. Sahar ND, Hong SI, Kohn DH. Micro- and nano-structural analyses of damage in bone. Micron 2005;36:617. [PubMed: 16169739]
32. Weiner S, Wagner HD. The material bone: Structure-mechanical function relations. Annu Rev Mater Sci 1998;28:271.
33. Khan, K.; McKay, H.; Kannus, P.; Bailey, D.; Wark, J.; Bennel, K. Physical Activity and Bone Health. Human Kinetics; Champaign, IL: 2001. p. 16
34. Martin, RB.; Burr, DB.; Sharkey, NA. Skeletal Tissue Mechanics. Springer; New York: 1998. p. 227
35. Rubin MA, Jasiuk I, Taylor J, Rubin J, Ganey T, Apkarian RP. TEM analysis of the nanostructure of normal and osteoporotic human trabecular bone. Bone 2003;33:270. [PubMed: 13678767]
36. Landis WJ, Song MJ, Leith A, McEwen L, McEwen BF. Mineral and organic interaction in normally calcifying tendon visualized in three dimensions by high volatage electron microscopic tomography and graphic imaging reconstruction. J Struct Biol 1993;110:39. [PubMed: 8494671]
37. Griffith AA. The phenomena of rupture and flow in solids. Philos Trans R Soc London, Ser A 1920;221:163.
38. Hong SI, Suryanarayana C. Is ductilization of intermetallic compounds by nanostructure processing a possibility? Mater Trans, JIM 2001;42:502.
39. Rohanizadeh R, LeGeros RZ, Bohie S, Pilet P, Barbier A, Daculsi G. Ultrastructural properties of bone mineral of control and tiludronate-treated osteoporotic rat. Calcif Tissue Int 2000;67:330. [PubMed: 11000348]
40. Kohn, DH.; Sahar, ND.; Hong, SI.; Golcuk, K.; Morris, MD. Local mineral and matrix changes associated with bone adaptation and microdamage*Mechanical Behavior of Biological and Biomimetic Materials*. In: Bushby, AJ.; Ferguson, VL.; Ko, CC.; Oyen, ML., editors. Mater Res Soc Symp Proc. Vol. 898E. Warrendale, PA: 2006. p. 0898-L09-03
41. Zaffe D. Some consideration on biomaterials and bone. Micron 2005;36:583. [PubMed: 16169740]
42. Dorozhkin SV. Calcium orthophosphates. J Mater Sci 2007;42:1061.
43. Rho JY, Kuhn-Spearing L, Zioupos P. Mechanical properties and the hierarchial structure of bone. Med Eng Phys 1998;20:92. [PubMed: 9679227]

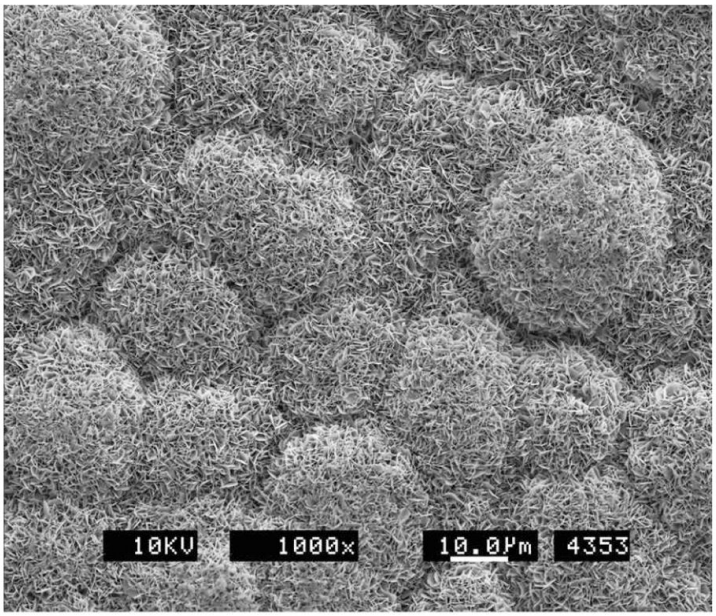

(a)

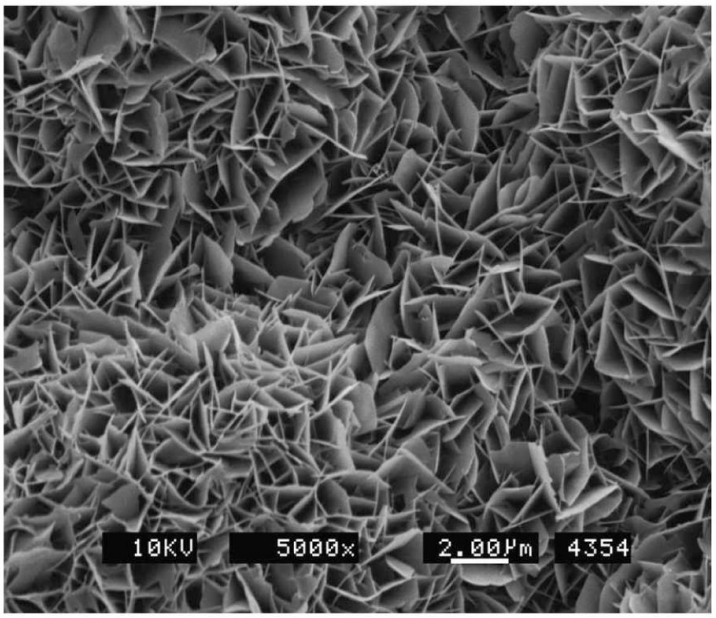

(b)

FIG. 1.

SEM micrographs of carbonated apatite deposits on PLGA substrates. (a) At a low magnification, a conglomerated granular structure with needle-shaped precipitates was clearly visible. (b) At a higher magnification, the surface was found to consist of elongated plates grown out of the surface of the granular structure.

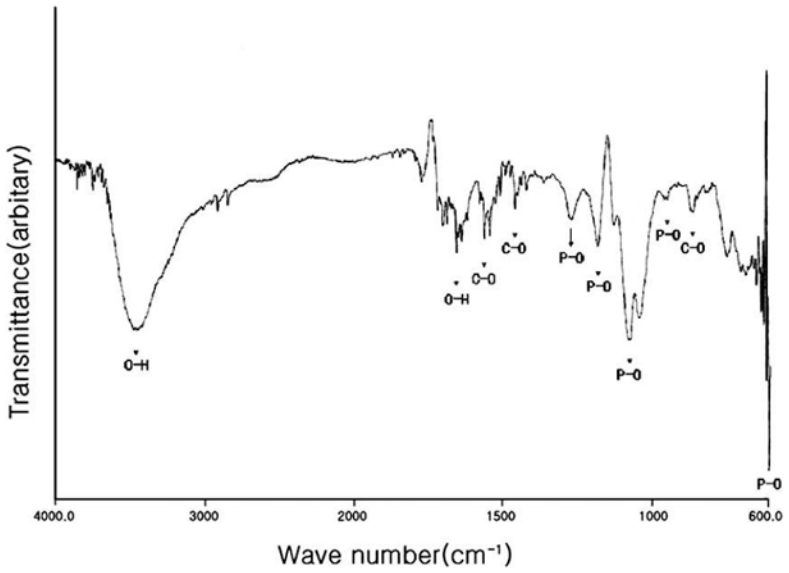

FIG. 2.
FTIR spectra of the carbonated apatite deposits.

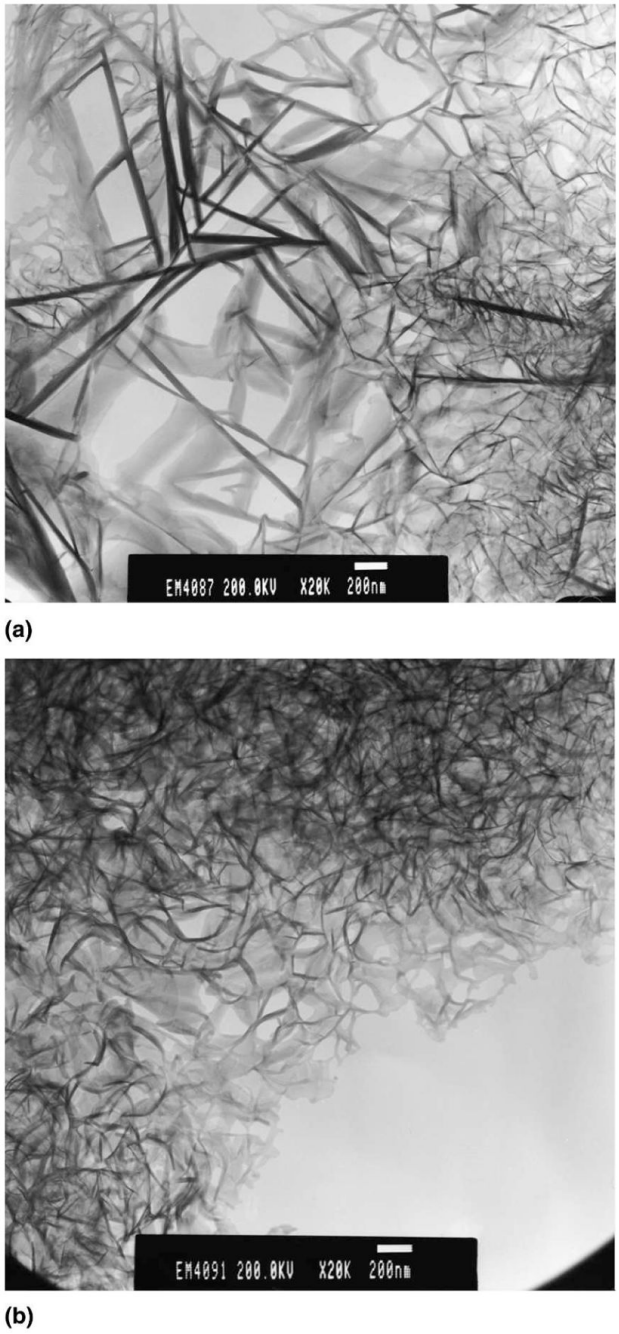

FIG. 3.

Ultrastructure of the carbonated apatite deposits observed by HRTEM, showing needlelike apatite with needle lengths ranging between 100 and 1000 nm. (a) The longer apatite needles (~1000 nm) were observed to be straight, whereas (b) smaller needles (~100–200 nm) were curved.

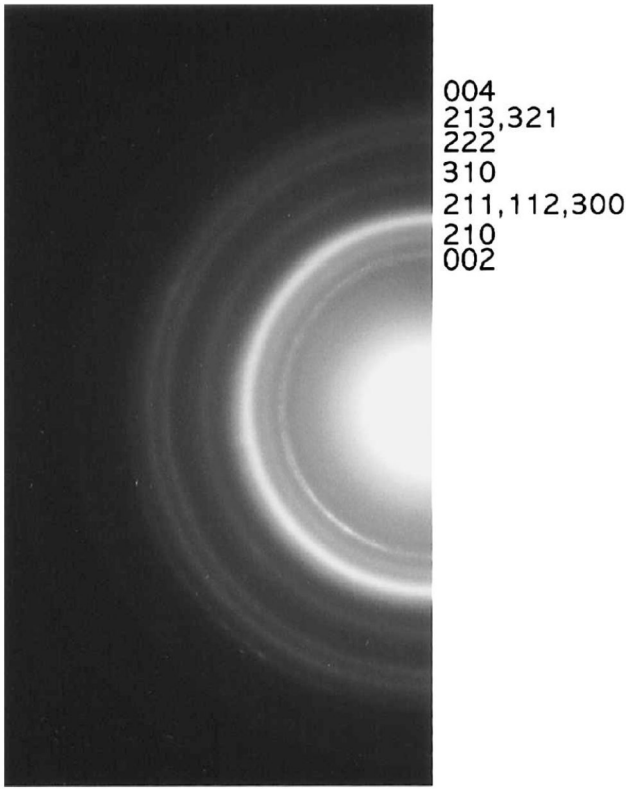

FIG. 4.

Diffraction pattern from carbonated apatite deposits. The pattern matched with indices obtained from HA. The change of lattice constants for the carbonated apatite with 3–8% carbonate substitution is so small that a difference in diffraction patterns between HA and carbonated apatite could not be identified. The continuous rings suggest that the coating consists of a great number of different crystals.

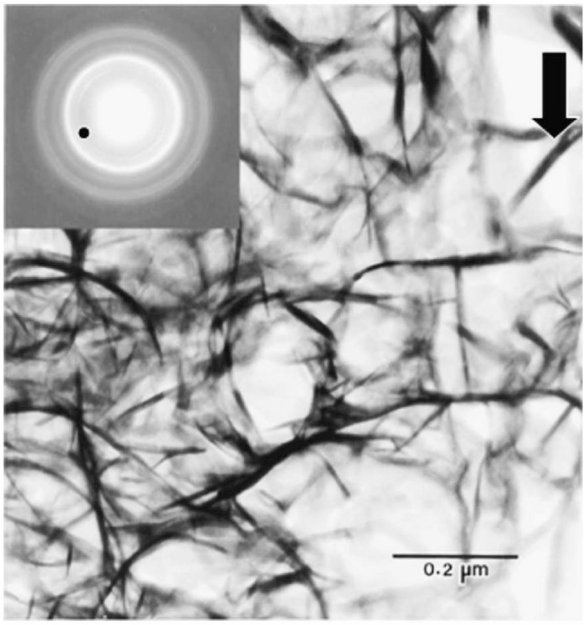

(a)

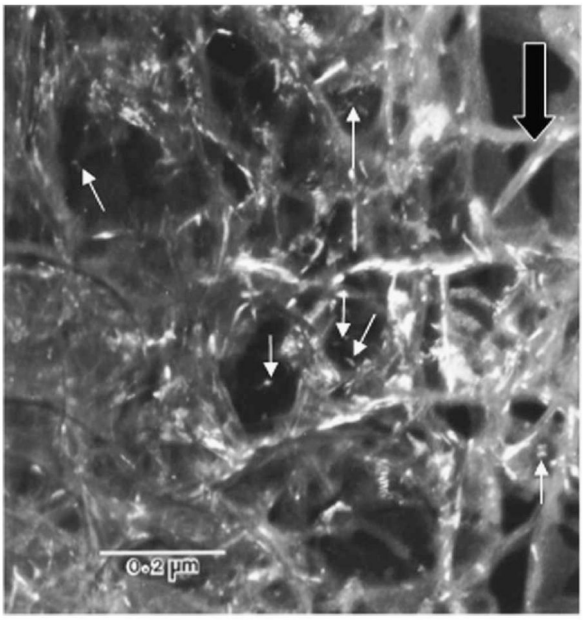

(b)

FIG. 5.

(a) Bright-field and (b) dark-field images taken from the same area. The dark-field image in (b) was obtained by placing the objective aperture on the spot of the (002) ring in the inset diffraction pattern of (a). Black arrow refers to needles that have ⟨002⟩ direction parallel to the plane; white arrows refer to small circular grains with crystalline orientation similar to that of the needles.

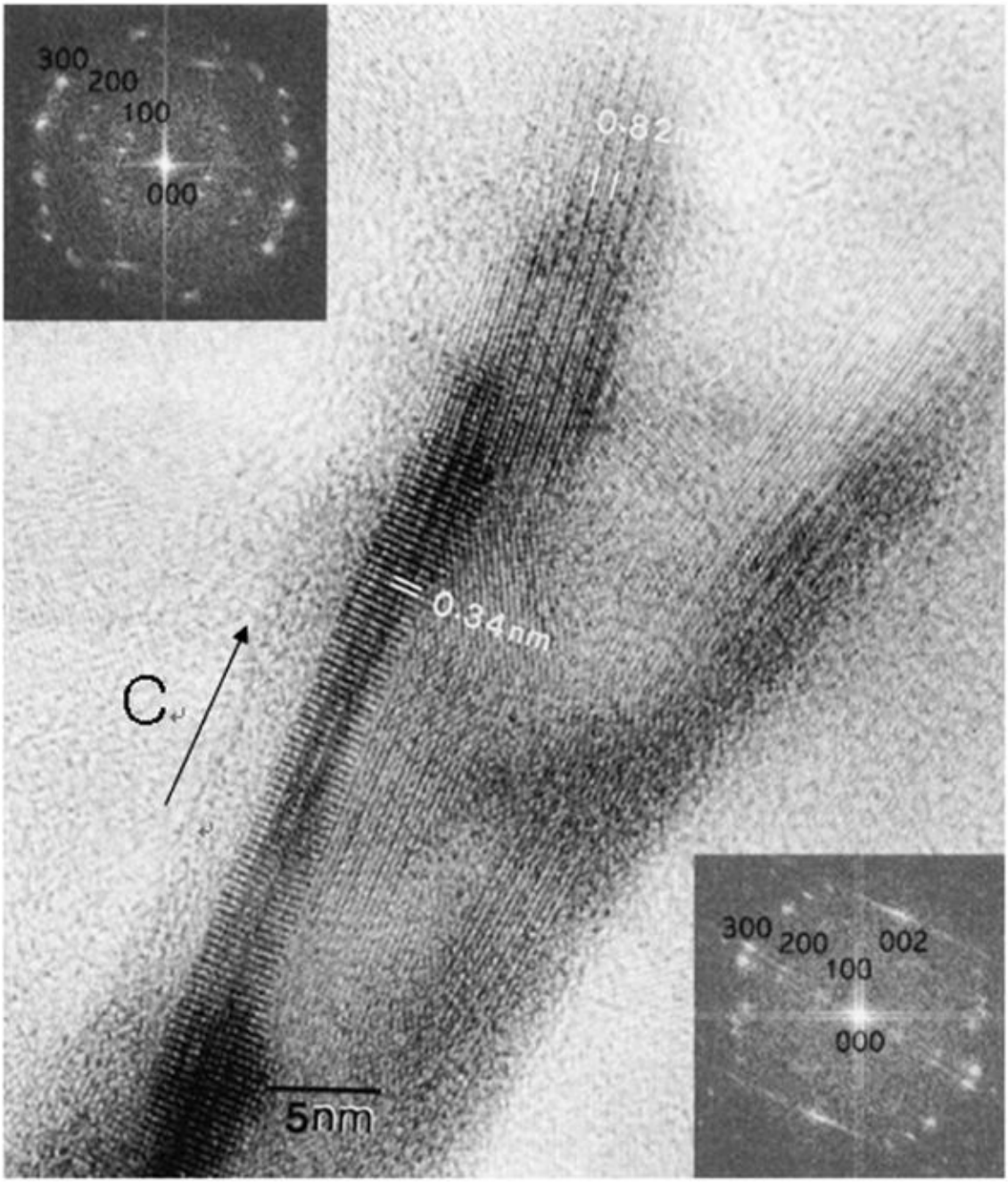

FIG. 6.

HRTEM image of scissor-shaped carbonated apatite. A crystalline lattice image is clearly visible in the needle, and the axis of each needle was parallel to the *c* axis [(002) direction] of the hexagonal structure.

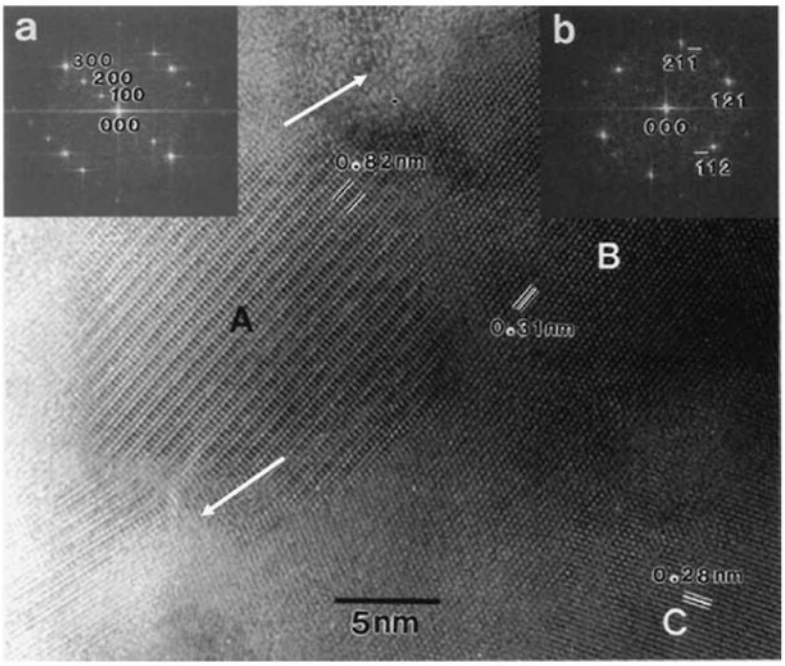

FIG. 7.

High-magnification image of a region surrounded by needles exhibits some granular apatites The FFT patterns from grains A and B revealed that the zone axis of grain A is [110] and that of grain B is [013]. Regions of ACP are indicated by the arrows.

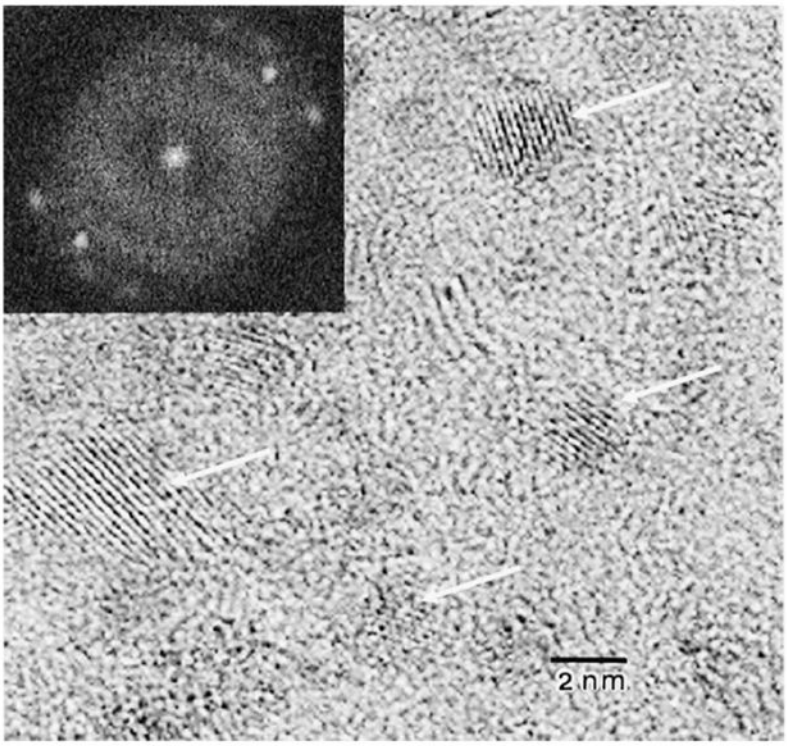

FIG. 8.
HRTEM image of ACP region with small crystalline apatite particles. Inset: FFT pattern.